Liquid-bridge breakup in contact-drop dispensing: Liquid-bridge stability with a free contact line

Amir Akbari and Reghan J. Hill*
Department of Chemical Engineering, McGill University, Montreal, Quebec, Canada H3A 0C5

Theo G. M. van de Ven
Department of Chemistry, McGill University, Montreal, Quebec, Canada H3A 2A7
(Received 19 January 2015; published 10 August 2015)

The static stability of weightless liquid bridges with a free contact line with respect to axisymmetric and nonaxisymmetric perturbations is studied. Constant-volume and constant-pressure stability regions are constructed in slenderness versus cylindrical volume diagrams for fixed contact angles. Bifurcations along the stability-region boundaries are characterized by the structure of axisymmetric bridge branches and families of equilibria. A wave-number definition is presented based on the pieces-of-sphere states at branch terminal points to classify equilibrium branches and identify branch connections. Compared with liquid bridges pinned at two equal disks, the free contact line breaks the equatorial and reflective symmetries, affecting the lower boundary of the constant-volume stability region where axisymmetric perturbations are critical. Stability is lost at transcritical bifurcations and turning points along this boundary. Our results furnish the maximum-slenderness stability limit for drop deposition on real surfaces when the contact angle approaches the receding contact angle.

DOI: 10.1103/PhysRevE.92.022404 PACS number(s): 68.05.−n, 68.03.−g, 68.08.−p

I. INTRODUCTION

Recent advances in nanoprinting and nanolithography [1–3] have provided new directions for studying liquid bridges. These techniques are the basis for nanoarray fabrication, which is central to data storage, pharmaceutical screening and detection, proteomics, and genotyping [1,4–6]. Crystal growth in microgravity [7], oil recovery [8], and elastocapillarity [9–12] are other applications where liquid-bridge stability and breakup are of interest. The ever-shrinking trend in electronic and diagnostic devices requires novel molecular-resolution and cost-effective patterning techniques. Direct-write constructive lithographic tools have been developed over the past decade to address this demand [1,13]. Contact-drop dispensing is the basis of several direct-write lithographic techniques, such as dip-pen nanolithography [14] and polymer pen lithography [2].

Liquid bridges in contact-drop dispensing feature a moving contact line. Although contact-drop dispensing is a dynamic process, the scaled form of the slender-jet approximation [15] suggests that the bridge profile can be accurately predicted by the Young-Laplace equation for small capillary numbers ($\mathrm{Ca} \ll 1$) [16,17]. However, liquid flow and contact-line motion become significant in a fast-dynamics phase preceding the pinchoff, affecting the bridge profile and dispensed drop volume [18]. The receding contact angle, contact-angle hysteresis, and needle retraction speed have been identified as the contributing parameters in the literature [18–22]. Here a crucial question arises as to what extent surface hydrophobicity, moving contact line, and needle retraction speed each contribute to the dispensed drop size. In contrast to previous studies, this paper focuses on the static stability limits of liquid bridges with a free contact line, on a surface with prescribed hydrophobicity, thus isolating the role of static parameters from dynamic ones.

Most previous studies have addressed the stability of liquid bridges pinned at both contact lines [23–32]. These studies, reviewed in detail by Akbari [33], examine the effect of several symmetry-breaking factors and external forces (e.g., unequal supports, centrifugal, and gravitational forces) on the stability region[1] of weightless liquid bridges spanning two circular disks. The lower and upper boundaries of the stability region are usually represented with respect to the cylindrical volume V and slenderness Λ (bridge-height to disk-radius ratio). These correspond, respectively, to the minimum- and maximum-volume stability limits at fixed slenderness.[2] However, the symmetry-breaking effect of a free contact line arising in contact-drop dispensing on stability has not been studied in the literature.

When losing stability, the nature of instabilities at critical equilibrium states has significant implications for the dynamics and evolution of capillary surfaces. The stability-region boundaries correspond to critical states at which continuous branch continuation is not uniquely possible [24,34], and the equilibrium branches bifurcate. Depending on the structure of the potential energy, this may result in a hard, soft-dangerous, or soft-safe stability loss [24]. Slobozhanin *et al.* [35] examined the bifurcation of weightless liquid bridges between equal disks along the entire stability-region boundaries. For a fixed Λ, axisymmetric bridges lose stability to nonaxisymmetric perturbations with increasing the cylindrical volume V at a supercritical (subcritical) bifurcation along the stability-region upper boundary when $\Lambda > 0.4946$ ($\Lambda < 0.4946$).

*reghan.hill@mcgill.ca

[1]Unless stated otherwise, stability region refers to the stability region with respect to constant-volume perturbations.

[2]Note that the maximum-volume stability limit at fixed slenderness, referred to as the rotund limit, is equivalent to the minimum-slenderness stability limit at fixed volume. Similarly, the minimum-volume stability limit at fixed slenderness, referred to as the slender limit, is equivalent to the maximum-slenderness stability limit at fixed volume.

 ©2015 American Physical Society

Axisymmetric bridges experience a soft-safe stability loss at supercritical pitchforks, leading to a continuous deformation to nonaxisymmetric shapes with incremental increase in volume, whereas they undergo a hard stability loss at subcritical pitchforks, resulting in a sharp, discontinuous deformation to nonaxisymmetric shapes. Here axisymmetric bridges seek the closest stable and dynamically accessible nonaxisymmetric configurations. This was proved to be in quantitative agreement with experimental observations [35,36]. Similarly, axisymmetric bridges lose stability at supercritical and subcritical pitchfork bifurcations to nonaxisymmetric perturbations along the lower boundary for small slendernesses. However, this results in contact-line detachment due to the geometric constraints [25,37]. At larger slendernesses, axisymmetric bridges lose stability to axisymmetric perturbations at turning points (subcritical pitchforks) for $\Lambda < 2.13$ ($\Lambda > 2.13$). This is a hard stability loss, causing the bridge to break into two primary drops. The lower boundary of the stability region (slender limit) is of particular interest to contact-drop dispensing where the drop volume is to be controlled. Here critical perturbations are reflectively symmetric (antisymmetric) at turning points (pitchforks) resulting in the formation of two equal (unequal) primary drops upon breakup [37].

Having a free contact line, liquid bridges in contact-drop dispensing are expected to exhibit a different behavior than those considered in the foregoing studies. Equilibrium solutions and their stability are affected through the integration constants of the Young-Laplace equation and the boundary conditions of the corresponding Sturm-Liouville problem, respectively. The latter has not been fully appreciated in the literature. Dodds *et al.* [17] examined the dynamics of stretching liquid bridges with two free contact lines between plates and cavities. The breakup length is then compared to Plateau's stability limit for a cylinder spanning the same support plates with the same radius as the bridge neck, providing an upper bound on the capillary number for which the quasistatic assumption is valid. However, the contact-line influence on the cylinder static stability limit is neglected, noting that the critical slenderness for cylinders with a free contact line and two free contact lines is less than Plateau's stability limit by $\sim 30\%$ [38] and 50% [39], respectively. In another paper, Qian and Breuer [40] studied the breakup dynamics of stretching liquid bridges having a pinned or free contact line with a substrate. The static stability limit was determined for selected bridge volumes and contact angles as a benchmark for dynamic results, without constructing the stability region. They experimentally identified the static stability limit when the contact line was free.

In this paper, we examine the static stability of weightless liquid bridges with a free contact line with respect to axisymmetric and nonaxisymmetric perturbations. We construct the constant-volume and constant-pressure stability regions in a broad contact-angle range from hydrophilic to hydrophobic. The stability region is presented in slenderness versus cylindrical volume diagrams with respect to constant-volume and constant-pressure perturbations. Bifurcations along the stability-region boundaries are characterized from the structure of axisymmetric bridge branches and families of equilibria, similarly to Lowry and Steen [27]. We also modify Lowry and Steen's wave-number classification and pieces-of-sphere configurations [27] to account for the symmetry-breaking effect of the free contact line. Pieces-of-sphere configurations are the states at the terminal points of equilibrium solution branches (except the rotund limit of the primary branch where the terminal point corresponds to a bulged nodoid), which can serve as the starting point in branch continuation techniques. Moreover, approximate expressions for the upper and lower boundaries of the stability region in the small slenderness limit are presented and compared with available formulas in the literature for liquid bridges between equal disks. Our results distinguish the symmetry-breaking and destabilizing effects of a free contact line with respect to liquid bridges between equal disks [27,35,39], unequal disks [26], and parallel plates [39,41,42], which have not been previously addressed. Controllable microdeposition benefits from the asymmetric breakup of liquid bridges. Hence, these effects, although static and geometric in nature, are of significant interest to contact-drop dispensing.

II. THEORY

We consider a liquid of volume v bridging a circular disk with radius R_0 and a large plate. The disk and plate are separated by a distance h, as shown in Fig. 1. The region occupied by the liquid bridge is denoted Ω_l, and that occupied by the surrounding fluid Ω_g. The bridge is pinned to the disk and is free to slide horizontally on the plate. The gravity force is neglected in this analysis, which is a reasonable approximation when the fluids are in microgravity (Bo $\ll 1$), the bridge dimensions are much smaller than the capillary length ($R_0, h \ll \sqrt{\gamma_{gl}/g|\rho_l - \rho_g|}$), or their densities are perfectly matched. Consequently, there is a constant pressure differential between the nonhydrostatic pressure of the bridge p_l and the surrounding fluid p_g. The origin of the coordinate system is placed on the bridge equatorial plane such that the z axis is the symmetry axis. The meridian curve is parametrized with respect to its arclength s. Axisymmetric equilibrium surfaces are specified by

$$r = r(s), \quad z = z(s), \quad s \in [s_0, s_1], \tag{1}$$

which are the stationary points of the energy functional

$$U[r(s), z(s)] = \gamma_{sl}\Gamma_{sl} + \gamma_{gl}\Gamma_{gl} + \gamma_{sg}\Gamma_{sg}, \tag{2}$$

where γ_{ij} is the surface tension between the phases i and j, and Γ_{ij} is the interfacial surface area. This is an isoperimetric variational problem for volume-controlled bridges and the extremization is subject to $v[r(s), z(s)] = \text{const}$. In contrast, pressure-controlled bridges are unconstrained. However, the pressure-work contribution to the energy functional due to volume changes must be accounted for. Therefore, the energy functional to be extremized in both pressure-controlled (unconstrained) and volume-controlled (constrained) cases is

$$F[r(s), z(s)] = U[r(s), z(s)] - (p_l - p_g)v[r(s), z(s)]. \tag{3}$$

The corresponding Euler-Lagrange equation is the well-known Young-Laplace equation

$$r'' = -z'(q - z'/r), \quad z'' = r'(q - z'/r) \,(' \equiv d/ds) \tag{4}$$

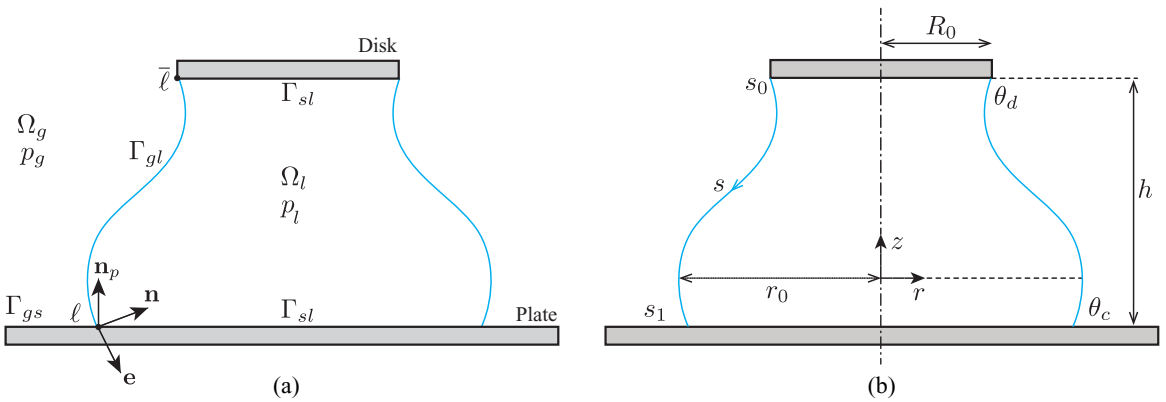

FIG. 1. (Color online) Weightless liquid bridge: (a) schematic and (b) coordinate system with meridian curve parametrization.

with

$$\gamma_{gl}\cos\theta_c = \gamma_{sl} - \gamma_{sg}, \quad \cos\theta_c = \mathbf{n}\cdot\mathbf{n}_p, \tag{5}$$

where $q = (p_g - p_l)/\gamma_{gl}$ measures the nonhydrostatic pressure differential (or mean curvature) [24]. Here θ_c and θ_d are the contact and dihedral angles that the interface Γ_{gl} forms with the plate and disk, respectively. Equilibrium solutions belong to the families of doubly connected, constant-mean curvature axisymmetric surfaces, including cylinders, spheres, catenoids, nodoids, and unduloids. The catenoid is a limiting case of the nodoid and unduloid family as $q \to 0$. The scaled lengths

$$\rho = |q|r, \quad \xi = qz, \quad \tau = |q|s \tag{6}$$

are adopted when $q \neq 0$ to nondimensionalize the Young-Laplace equation, furnishing

$$\rho'' = -\xi'(1 - \xi'/\rho), \quad \xi'' = \rho'(1 - \xi'/\rho)\,(' \equiv d/d\tau) \tag{7}$$

with

$$\rho(0) = \rho_0, \quad \rho'(0) = 0, \quad \xi(0) = 0, \quad \xi'(0) = 1. \tag{8}$$

The cylindrical volume $V = v/\pi R_0^2 h$, scaled volume $v^* = v/4\pi R_0^3/3$, scaled pressure (mean curvature) $Q = qR_0$, and slenderness $\Lambda = h/R_0$ are the dimensionless parameters adopted in this paper to present the stability region and branching diagrams.

The stability region for constant-volume perturbations has a more complicated structure than at constant pressure. The entire upper boundary and part of the lower boundary correspond to pitchfork bifurcations where nonaxisymmetric perturbations are critical. Axisymmetric perturbations are critical along the lower boundary for longer liquid bridges, and the stability loss occurs at turning points and transcritical bifurcations. Hence, to capture these complexities, we apply the variational method of Myshkis *et al.* [24] to determine the stability of equilibrium surfaces with respect to arbitrary volume-preserving perturbations. This method associates the second variation of the potential energy with the eigenvalues of the corresponding spectral (Sturm-Liouville) problem where critical states satisfy

$$\begin{gathered} \mathscr{L}\varphi_0 + \mu = 0, \quad \varphi_0(\tau_0) = 0, \\ \varphi_0'(\tau_1) + \tilde{\chi}\varphi_0(\tau_1) = 0, \quad \int_{\tau_0}^{\tau_1} \rho\varphi_0 d\tau = 0 \end{gathered} \tag{9}$$

for axisymmetric perturbations and

$$(\mathscr{L} - 1/\rho^2)\varphi_1 = 0, \quad \varphi_1(\tau_0) = 0, \quad \varphi_1'(\tau_1) + \tilde{\chi}\varphi_1(\tau_1) = 0 \tag{10}$$

for nonaxisymmetric perturbations. Here $\tau_0 = |q|s_0$, $\tau_1 = |q|s_1$,

$$\chi = \frac{k_{1\ell}\cos\theta_c - k_{p\ell}}{\sin\theta_c} \quad \text{at } \ell, \tag{11}$$

and

$$\mathscr{L} \equiv \frac{d^2}{d\tau^2} + \frac{\rho'}{\rho}\frac{d}{d\tau} + \left[\left(1 - \frac{\xi'}{\rho}\right)^2 + \left(\frac{\xi'}{\rho}\right)^2\right] \tag{12}$$

with $\tilde{\chi} = \chi/|q|$; the first principal curvature of the interface and plate at the contact line ℓ are denoted $k_{1\ell}$ and $k_{p\ell}$, respectively. Note that $\varphi_0(\tau)$ and $\varphi_1(\tau)$ represent the axisymmetric and nonaxisymmetric perturbations corresponding to the first harmonic mode in θ. The solutions of Eqs. (9) and (10) can be written

$$\varphi_0(\tau) = C_1 w_1(\tau) + C_2 w_2(\tau) + \mu w_3(\tau), \tag{13}$$

$$\varphi_1(\tau) = C_4 w_4(\tau) + C_5 w_5(\tau). \tag{14}$$

These satisfy the following differential equations and their initial conditions:

$$\mathscr{L}w_1 = 0, \quad w_1(0) = 0, \quad w_1'(0) = 1, \tag{15}$$

$$\mathscr{L}w_2 = 0, \quad w_2(0) = 1, \quad w_2'(0) = 0, \tag{16}$$

$$\mathscr{L}w_3 + 1 = 0, \quad w_3(0) = 1, \quad w_3'(0) = 0, \tag{17}$$

$$(\mathscr{L} - 1/\rho^2)w_4 = 0, \quad w_4(0) = 0, \quad w_4'(0) = 1, \tag{18}$$

$$(\mathscr{L} - 1/\rho^2)w_5 = 0, \quad w_5(0) = 1, \quad w_5'(0) = 0. \tag{19}$$

An equilibrium-surface state is critical if φ_0 or φ_1 has a nontrivial solution. It can be shown that a nontrivial solution

for φ_0 (φ_1) exists provided $\tilde{\chi} = \tilde{\chi}^0$ ($\tilde{\chi} = \tilde{\chi}^1$), where

$$\tilde{\chi}^0 = -\frac{\begin{vmatrix} w_1(\tau_0) & w_2(\tau_0) & w_3(\tau_0) \\ w_1'(\tau_1) & w_2'(\tau_1) & w_3'(\tau_1) \\ \int_{\tau_0}^{\tau_1} \rho w_1 d\tau & \int_{\tau_0}^{\tau_1} \rho w_2 d\tau & \int_{\tau_0}^{\tau_1} \rho w_3 d\tau \end{vmatrix}}{\begin{vmatrix} w_1(\tau_0) & w_2(\tau_0) & w_3(\tau_0) \\ w_1(\tau_1) & w_2(\tau_1) & w_3(\tau_1) \\ \int_{\tau_0}^{\tau_1} \rho w_1 d\tau & \int_{\tau_0}^{\tau_1} \rho w_2 d\tau & \int_{\tau_0}^{\tau_1} \rho w_3 d\tau \end{vmatrix}}, \quad (20)$$

$$\tilde{\chi}^1 = -\frac{\begin{vmatrix} w_4(\tau_0) & w_5(\tau_0) \\ w_4'(\tau_1) & w_5'(\tau_1) \end{vmatrix}}{\begin{vmatrix} w_4(\tau_0) & w_5(\tau_0) \\ w_4(\tau_1) & w_5(\tau_1) \end{vmatrix}} \quad (21)$$

with $\tilde{\chi}^0$ and $\tilde{\chi}^1$ the critical $\tilde{\chi}$ corresponding to axisymmetric and nonaxisymmetric perturbations, respectively. One can deduce from the properties of the spectral problem that an equilibrium surface is stable (unstable) if $\tilde{\chi} > \max\{\tilde{\chi}^0, \tilde{\chi}^1\}$ ($\tilde{\chi} < \max\{\tilde{\chi}^0, \tilde{\chi}^1\}$), and it is in a critical state when $\tilde{\chi} = \max\{\tilde{\chi}^0, \tilde{\chi}^1\}$. Details of this method are given by Myshkis *et al.* [24].

The critical-state criterion $\tilde{\chi} = \max\{\tilde{\chi}^0, \tilde{\chi}^1\}$ defines a boundary between the stability region and its complement in the space of physical parameters that the system depends on. Because this nonlinear equation has multiple solutions, it is necessary to restrict the search for critical states to a region that can be systematically constructed. The maximal stability region (MSR), a concept introduced by Slobozhanin and Tyuptsov [43], addresses this need. The critical states associated with the MSR are determined by

$$D^0 = \begin{vmatrix} w_1(\tau_0) & w_2(\tau_0) & w_3(\tau_0) \\ w_1(\tau_1) & w_2(\tau_1) & w_3(\tau_1) \\ \int_{\tau_0}^{\tau_1} \rho w_1 d\tau & \int_{\tau_0}^{\tau_1} \rho w_2 d\tau & \int_{\tau_0}^{\tau_1} \rho w_3 d\tau \end{vmatrix}, \quad (22)$$

$$D^1 = \begin{vmatrix} w_4(\tau_0) & w_5(\tau_0) \\ w_4(\tau_1) & w_5(\tau_1) \end{vmatrix}. \quad (23)$$

For a fixed τ_0, the first τ_1 along the meridian curve at which $D^0 = 0$ ($D^1 = 0$) corresponds to a critical state of the MSR with respect to axisymmetric (nonaxisymmetric) perturbations. Thus, one needs to seek nontrivial solutions of $\tilde{\chi} = \max\{\tilde{\chi}^0, \tilde{\chi}^1\}$ only for surfaces belonging to the MSR. All equilibrium surfaces outside the MSR are unstable.

The entire stability-region boundary for constant-pressure perturbations correspond to simple turning points in pressure. Hence, Maddocks' theorem can be applied to deduce stability from the structure of equilibrium branches in volume-pressure diagrams without additional analysis [44]. This theorem can be rephrased as follows: Stability exchange only occurs at simple turning points for equilibrium branches without bifurcation points. Results are independent of the meridian curve boundary conditions and thus are applicable to liquid bridges with free and pinned contact lines. The stability of the segment confined between the two pressure turning points is inferred from the truncated sphere stability. Moreover, it immediately follows from Maddocks' theorem that the two branch segments beyond the turning points correspond to bridges that are unstable to constant-pressure perturbations.

III. RESULTS AND DISCUSSION

A. Equilibrium branch construction

Solving Eq. (7) with the initial conditions of Eq. (8) furnishes the equilibrium meridian curve [24]

$$\rho(\tau) = \sqrt{1 + a^2 + 2a\cos\tau}, \quad \xi(\tau) = \int_0^\tau \frac{1 + a\cos t}{\rho(t)} dt, \quad (24)$$

giving

$$|Q| = \sqrt{1 + a^2 + 2a\cos\tau_0}, \quad (25)$$

$$\Lambda = -\frac{1}{Q}\int_{\tau_0}^{\tau_1} \frac{1 + a\cos t}{\rho(t)} dt, \quad (26)$$

$$\tan\theta_d = \mathrm{sgn}(Q)\frac{1 + a\cos\tau_0}{a\sin\tau_0}, \quad (27)$$

$$\tan\theta_c = -\mathrm{sgn}(Q)\frac{1 + a\cos\tau_1}{a\sin\tau_1}, \quad (28)$$

$$V = -\frac{1}{Q^3\Lambda}\int_{\tau_0}^{\tau_1} \rho(t)(1 + a\cos t) dt, \quad (29)$$

where $a = \rho(0) - 1$. Equations (25)–(29) furnish five constraints on τ_0, τ_1, a, Q, Λ, V, θ_c, and θ_d, leaving three degrees of freedom. The last five variables are single-valued functions of the first three. Consequently, fixing (τ_0, τ_1, a), an equilibrium state characterized by $(Q, \Lambda, V, \theta_c, \theta_d)$ is uniquely specified.[3] One can choose any set of three variables to specify equilibrium states; however, this uniqueness is not necessarily preserved. Hereafter, any chosen set is denoted **p** and will be referred to as independent parameters. The remaining variables are thereby termed dependent parameters or norms and are used as the ordinate in branching diagrams. The scaled volume v^* and cylindrical volume V can be interchanged without affecting the representation of equilibrium solution multiplicity. In this paper, we present equilibrium branches in (v^*, Q) diagrams for fixed Λ and θ_c and the stability region in (Λ, V) diagrams for fixed θ_c. Note that (v^*, Q) are the preferred coordinates in which stability limits can be associated with turning points for constant-volume and constant-pressure axisymmetric perturbations [44].

Solving Eqs. (25), (26), and (28), we choose $\mathbf{p} = (\tau_0, \tau_1, a)$ and Q as the branch parameter to construct equilibrium branches for fixed Λ and θ_c. This significantly reduces the computational cost as compared to problems in which the meridian curve is computed numerically. For example, Martínez and Perales [45] applied the same idea to construct equilibrium branches for liquid bridges pinned at two unequal disks and documented the minimum volume stability limit in terms of three physical parameters. The stability region and equilibrium branches are presented for $\mathbf{p} = (\Lambda, V, \theta_c)$. We use Keller's

[3] This does not imply that there is a one-to-one correspondence between (τ_0, τ_1, a) and equilibrium states. In fact, equilibrium meridian curves are invariant with respect to the transformation $\bar{\tau}_0 = \tau_0 + (2n-1)\pi$, $\bar{\tau}_1 = \tau_1 + (2n-1)\pi$, and $\bar{a} = -a$, with $n \in \mathbb{Z}$. All (τ_0, τ_1, a) satisfying this transformation specify identical equilibrium states and distinguishing them is insignificant.

arclength continuation method, as outlined by Seydel [34]. Branch continuation begins at a pieces-of-sphere state and terminates at another pieces-of-sphere state or a bulged nodoid with $\theta_d = -\pi$. Note that the liquid bridges in Fig. 1 are restricted by the geometric constraint $\theta_d \leqslant \pi$. This constraint is nevertheless relaxed to compute the entire equilibrium branch. However, we exclude self-intersecting meridian curves from equilibrium branches as they are nonphysical [46]. Of course, this constraint is automatically satisfied by limiting equilibrium branches between two pieces-of-sphere states.

B. Pieces-of-sphere configurations

Branch classification based on wave number plays a significant role in the bifurcation, dynamics, and breakup of liquid bridges. Several definitions have been proposed in the literature. The number of negative eigenvalues is associated with instability modes and thus is useful for applications in which suppression of instabilities is sought. This provides insight into possible ways of stabilizing liquid bridges [47]. Vogel [48] considered bridges with free contact lines between two parallel plates and defined the wave number n_w as the number of inflection points in the meridian curve. Here the wave number is invariant along branches with no bifurcation point when the contact angles are equal. Lowry and Steen [27] provided a definition for bridges pinned at two equal disks where the wave number is invariant for branches that do not intersect the $\cos\theta_d$ axis in V versus $\cos\theta_d$ diagrams. This intersection occurs at a pitchfork bifurcation where axisymmetric perturbations are critical. Here an even-wave-number branch intersects an odd-wave-number one. The number of extrema in the meridian curve is defined as the wave number in this case. They also showed that the latter two definitions are compatible with the constraints at the contact lines.

The free contact line of liquid bridges considered in this study breaks the equatorial symmetry. These bridges are subject to different constraints at the upper and lower contact lines and their equilibrium branches exhibit no particular invariance property. This is also reflected in the bifurcations along the stability-region lower boundary. Here branch intersections merely occur at transcritical bifurcations. Moreover, one can show by counterexample that neither the number of inflection points nor the number of extrema is invariant along equilibrium branches. In this work, the wave-number definition is based on the pieces-of-sphere configurations at the terminal points, which is used to label equilibrium branches. The wave number is invariant along each disconnected branch. For a given θ_c, there is a slenderness at which n_w and $n_w - 1$ branches intersect at a transcritical bifurcation (n_w being even). Beyond this slenderness, the transcritical bifurcation breaks into two folds where even- and odd-wave-number half branches meet. Here the wave number is invariant along half branches, from the pieces-of-sphere state at the terminal point to the corresponding fold. This is a suitable definition because the two folds arising from the unfolding of transcritical bifurcations are indicated by a wave-number transition.

We first demonstrate why equilibrium branches are limited by pieces-of-sphere configurations before formally defining the wave number for liquid bridges with a free contact line. Figure 2 shows how the meridian curves given by Eq. (24)

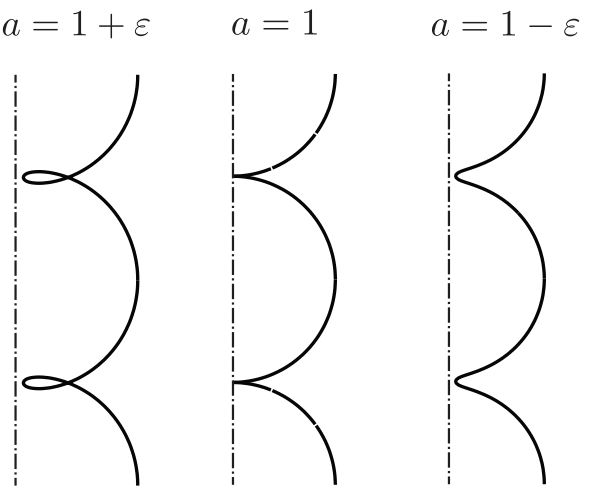

FIG. 2. Transition from a self-intersecting profile to a non-self-intersecting profile by varying the shape parameter a.

vary with the shape parameter a. Pieces-of-sphere states are the limiting case of nodoidal (self-intersecting) and unduloidal (non-self-intersecting) liquid bridges as $a \to 1$. Increasing (decreasing) a by a small value ε, a pieces-of-sphere state is transformed into a nodoid (an unduloid). Note how a self-intersecting profile approaches ($a > 1$) and touches ($a = 1$) the symmetry axis, unfolds, and detaches ($a < 1$) from it as a decreases in the region $|a - 1| < \varepsilon$. For a fixed Λ and θ_c, the meridian curve changes continuously with a along the equilibrium branch. Therefore, excluding self-intersecting profiles leaves branches that are terminated at pieces-of-sphere states.

The wave number for pieces-of-sphere states is defined as a positive integer such that it is even (odd) when all (one of) the points at which the meridian curve touches the symmetry axis lie(s) between the plate and disk (on the plate). Each complete (truncated) sphere in the chain of spheres spanning the disk and plate adds two (one) to the wave number. This definition is illustrated in Fig. 3, where $n_w = 1$ and $n_w = 2$ are the basic states for odd-wave-number and even-wave-number pieces-of-sphere states, respectively. These configurations can be specified analytically, furnishing a convenient starting point for branch continuation methods. We first present the solution of the basic states. Solutions for higher odd and even wave number immediately follow from the respective basic states. Denoting the slenderness and scaled arclength at the disk for the basic states by $\tilde{\Lambda}$ and $\tilde{\tau}_0$, respectively, the state $n_w = 1$ is specified by

$$\Lambda = \tilde{\Lambda}, \tag{30}$$

$$Q = -\frac{4\tilde{\Lambda}}{\tilde{\Lambda}^2 + 1}, \tag{31}$$

$$\tilde{\tau}_0 = 2\,\mathrm{arctan2}\left(-\frac{2\tilde{\Lambda}}{\tilde{\Lambda}^2 + 1}, -\frac{\tilde{\Lambda}^2 - 1}{\tilde{\Lambda}^2 + 1}\right) + \pi, \tag{32}$$

$$\tau_1 = \pi, \tag{33}$$

$$a = 1, \tag{34}$$

$$\theta_d = (\tilde{\tau}_0 + \pi)/2, \tag{35}$$

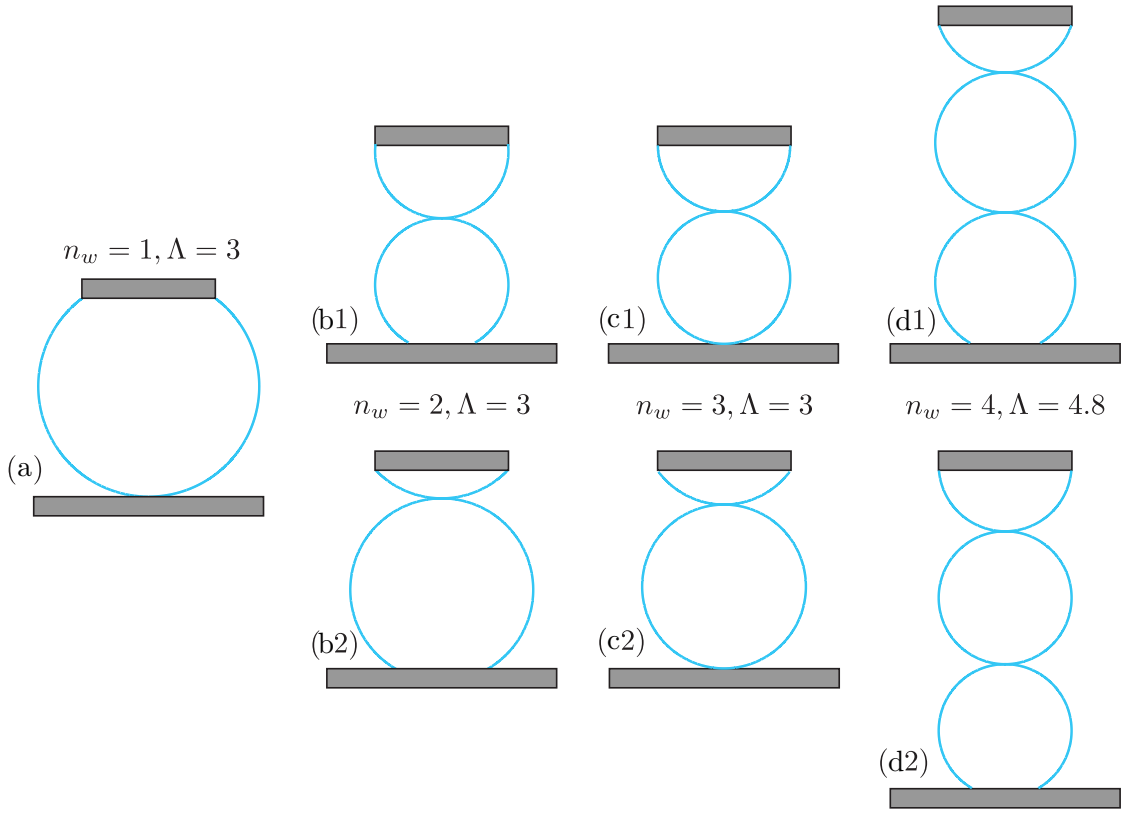

FIG. 3. (Color online) Wave-number definition based on pieces-of-sphere states for the contact angle $\theta_c = 30^\circ$.

where arctan2 is the four-quadrant inverse tangent. This state [Fig. 3(a)] exists for all Λ and is a terminal point of the primary branch. Note that Eqs. (31)–(35) are independent of θ_c, so $a \to 1$ as $\tau_1 \to \pi$ such that Eq. (28) is satisfied. Similarly, the state $n_w = 2$ is specified by

$$\Lambda = \tilde{\Lambda}, \tag{36}$$

$$Q = -2M, \tag{37}$$

$$\tilde{\tau}_0 = 2\,\mathrm{arctan2}(-M, -M\tilde{\Lambda} + \cos\theta_c + 2) + \pi, \tag{38}$$

$$\tau_1 = 3\pi - 2\theta_c, \tag{39}$$

$$a = 1, \tag{40}$$

$$\theta_d = (\tilde{\tau}_0 + \pi)/2 \tag{41}$$

with

$$M = \frac{\tilde{\Lambda}(\cos\theta_c + 2) \pm \sqrt{1 - (2 + \cos\theta_c)^2 + \tilde{\Lambda}^2}}{\tilde{\Lambda}^2 + 1}. \tag{42}$$

This state has two solutions corresponding to the two terminal points of the branch $n_w = 2$ [Figs. 3(b1) and 3(b2)] and exists for all $\Lambda > \Lambda^{(2)}$, where

$$\Lambda^{(2)} = \sqrt{(2 + \cos\theta_c)^2 - 1}. \tag{43}$$

Here $\Lambda^{(2)}$ is the slenderness at which the branch $n_w = 2$ originates. Unlike liquid bridges between equal disks, the two states corresponding to the terminal points of the branch $n_w = 2$ are not axial mirror images (no reflective symmetry). This reveals an intimate connection between pitchfork bifurcations and geometrical symmetry, as pointed out by Seydel [34]. The geometric idealization of liquid bridges pinned at perfectly equal disks is unlikely to be realized in practice. These axisymmetric liquid bridges are also equatorially or reflectively symmetric, the combination of which underlies the branch intersections at pitchfork bifurcations (nongeneric). Small changes in geometry and constraints destroy nongeneric bifurcations [34], which is why they are rarely, if at all, encountered in practical problems such as the one considered in this paper. The solution of higher odd-wave-number states is

$$\Lambda = \tilde{\Lambda} + \frac{(n_w - 1)(\tilde{\Lambda}^2 + 1)}{2\tilde{\Lambda}}, \tag{44}$$

$$\tau_0 = \tilde{\tau}_0 - n_w\pi, \tag{45}$$

where Q, τ_1, a, and θ_d are the same as for the basic state. These states are independent of θ_c and exist for all $\Lambda > \Lambda^{(n_w)}$, where

$$\Lambda^{(n_w)} = \sqrt{n_w^2 - 1}, \quad n_w \in \{3,5,7,\ldots\}. \tag{46}$$

Equation (44) has the solutions

$$\tilde{\Lambda} = \frac{\Lambda \pm \sqrt{\Lambda^2 - n_w^2 + 1}}{n_w + 1} \tag{47}$$

for a given Λ corresponding to the two terminal points of the respective branch [Figs. 3(c1) and 3(c2) for $n_w = 3$].

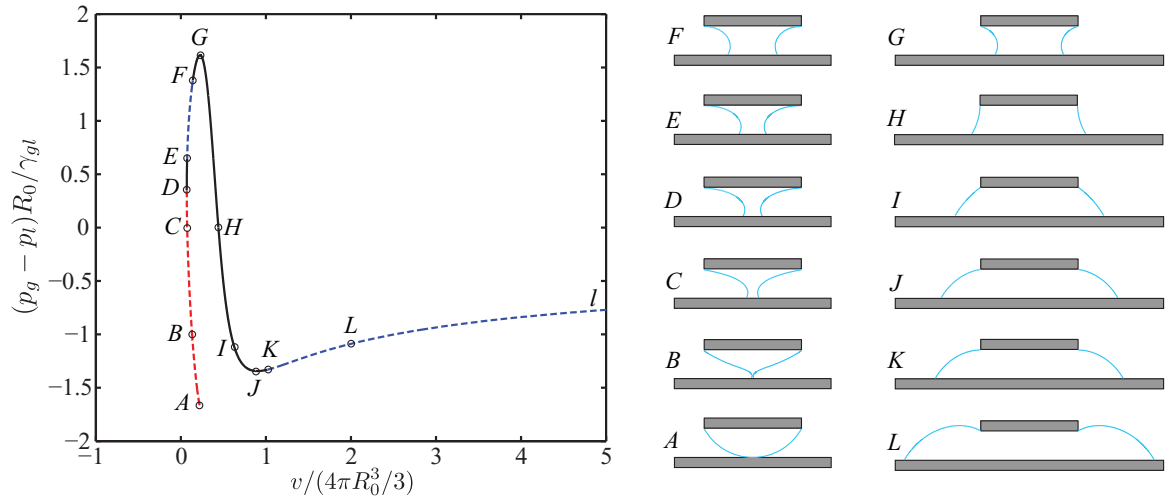

FIG. 4. (Color online) Equilibrium shapes along the equilibrium branch with the slenderness $\Lambda = 0.53$ and contact angle $\theta_c = 120^\circ$. Stable states (solid) and unstable states (dashed) to axisymmetric (red) and nonaxisymmetric (blue) perturbations are represented for constant-volume perturbations.

Similarly,

$$\Lambda = \tilde{\Lambda} + \frac{n_w - 2}{M}, \tag{48}$$

$$\tau_0 = \tilde{\tau}_0 - (n_w - 1)\pi \tag{49}$$

for higher even-wave-number states. These states depend on θ_c and exist for all $\Lambda > \Lambda^{(n_w)}$, where

$$\Lambda^{(n_w)} = \sqrt{n_w^2 + 2n_w \cos\theta_c + (\cos 2\theta_c - 1)/2},$$
$$n_w \in \{4,6,8,\ldots\}. \tag{50}$$

Equation (48) has the solutions

$$\tilde{\Lambda} = \frac{2n_w\Lambda(2+\cos\theta_c) + \Lambda(\cos 2\theta_c + 4\cos\theta_c - 1) \pm \sqrt{2}(n_w - 2)\sqrt{2\Lambda^2 + 1 - 2n_w^2 - 4n_w\cos\theta_c - \cos 2\theta_c}}{2n_w^2 + 4n_w\cos\theta_c + \cos 2\theta_c - 1} \tag{51}$$

for a given Λ, corresponding to the two terminal points of the respective branch [Figs. 3(d1) and 3(d2) for $n_w = 4$].

C. Stability of equilibrium branches

In this section, the typical behavior of equilibrium branches is illustrated based on the $n_w = 1$ and $n_w = 2$ branches. Except the primary branch ($n_w = 1$), all higher wave-number branches correspond to liquid bridges that are unstable to constant-volume and constant-pressure axisymmetric perturbations. The secondary branch ($n_w = 2$), however, plays an important role in constructing the stability region. In a certain range of Λ and θ_c, the secondary branch intersects the stable part of primary branches, splitting it into two disconnected stable segments. This appears as a kink in the stability-region lower boundary, which is similar to the one in the lower boundary for short bridges that correspond to critical states with respect to nonaxisymmetric perturbations.

Figure 4 shows how equilibrium shapes vary along a typical equilibrium branch for a fixed Λ and θ_c. At this slenderness, only the primary branch exists. The branch starts at a pieces-of-sphere state A and ends at a bulged nodoid[4] with $\theta_d = -\pi$ (not shown). The segment EF corresponds to bridges with $\theta_d > \pi$, which cannot be realized in practice between a disk and plate (see Fig. 1) due to the geometric constraint mentioned in the Introduction. Similar to bridges pinned at two equal disks, these are unstable to constant-volume nonaxisymmetric perturbations. The remaining stable segment DE loses stability at the volume turning point D to axisymmetric perturbations. The rotund limit K is a pitchfork bifurcation where stability is lost to nonaxisymmetric perturbations and the bridge is a nodoid with $\theta_d = 0$. Constant-pressure stability is determined by pressure turning points. There are two turning points in pressure (G and J) in Fig. 4 at which stability exchange occurs according to Maddocks' theorem. The truncated sphere state I belongs to the segment GJ, implying that it is a stable segment. Stability is lost at G and J to axisymmetric perturbations; thus, AG and Jl are unstable segments. Furthermore, two catenoids exist for the given Λ and θ_c [38], corresponding to the points C and H where $Q = 0$. The catenoid C (H) is unstable (stable) to both constant-volume and constant-pressure perturbations.

The segment AD belongs to the MSR with respect to axisymmetric perturbations and the minimum eigenvalue of the spectral problem considered by Qian and Breuer [40] is positive alone this branch. Therefore, neglecting the role of the free-contact line in the Sturm-Liouville problem results in the misidentification of the segment AD as a stable branch.

[4]What bulged and constricted mean here is not as evident as for bridges between equal disks. In this paper, bulged [constricted] bridges refer to surfaces with $r(s_1)/R_0 > 1$ [$r(s_1)/R_0 < 1$].

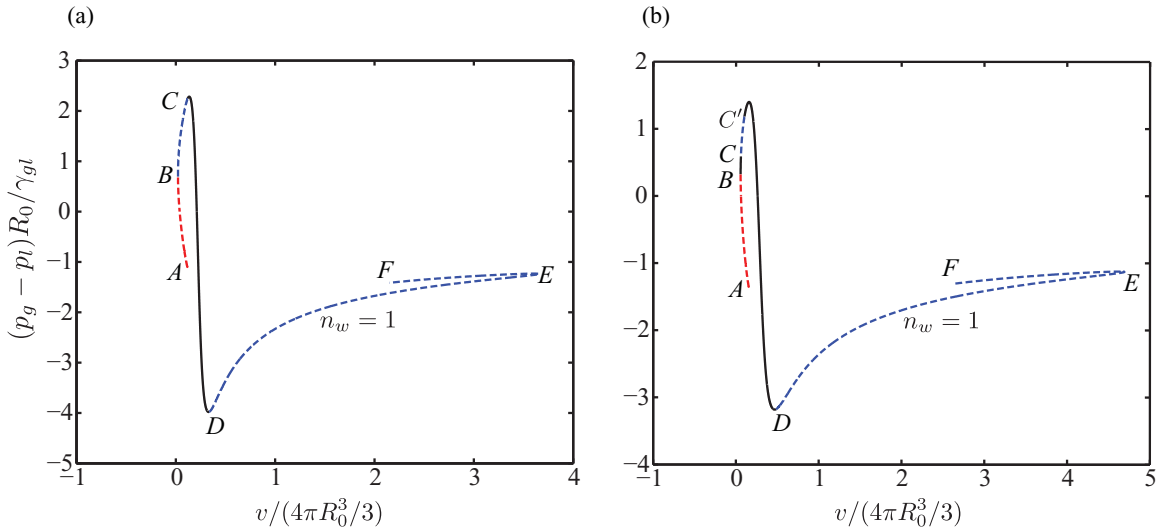

FIG. 5. (Color online) Equilibrium branch for short liquid bridges at fixed slenderness Λ and contact angle θ_c: (a) $\Lambda = 0.3$ and $\theta_c = 90^\circ$ and (b) $\Lambda = 0.39$ and $\theta_c = 90^\circ$. Stable states (solid) and unstable states (dashed) to axisymmetric (red) and nonaxisymmetric (blue) perturbations are represented for constant-volume perturbations.

The remainder of this section focuses on how equilibrium branches change with Λ for $\theta_c = 90^\circ$ as an example. This is the only contact angle that is compatible with cylindrical bridges and thus of particular interest. Figure 5 shows how equilibrium branches behave for short bridges. Here nonaxisymmetric perturbations are critical at the maximum and minimum volume stability limits. The secondary branch does not exist at these small slendernesses. For $\Lambda < 0.364$ [Fig. 5(a)], moving along the branch from D to A, the dihedral angle first exceeds π at C, but does not drop below π before the turning point B. Hence, there is one connected stable segment. At the rotund limit, constant-volume stability is lost to nonaxisymmetric perturbations at D where the bridge is a bulged nodoid with $\theta_d = 0$. At the slender limit, constant-volume stability is lost to nonaxisymmetric perturbations at C where the bridge is a constricted nodoid with $\theta_d = \pi$. At the volume turning point B, the nature of critical perturbations changes. Beyond this turning point, axisymmetric perturbations are the most dangerous along AB. Moreover, the two terminal points A and F correspond to a pieces-of-sphere and nodoid with $\theta_d = -\pi$, respectively. Note how this branch is limited by two volume and two pressure turning points. Constant-volume stability nevertheless cannot be determined from Maddocks' theorem since the branch has two bifurcation points between the turning points. However, Maddocks' theorem can be applied to constant-pressure stability. The segment between the pressure turning points has no bifurcation points and is stable to constant-pressure perturbations. For $0.364 < \Lambda < 0.404$ [Fig. 5(b)], equilibrium branches behave similarly to the previous case, except in the slender limit. Here the dihedral angle exceeds π along CC' where bridges are unstable to nonaxisymmetric perturbations. This results in two disconnected stable segments (BC and $C'D$).

Further increase in the slenderness significantly influences the behavior of equilibrium branches. No sign change occurs in the pressure differential along the branch when $\Lambda > 0.663$. Here there are no points on the branch corresponding to catenary profiles and Q is always negative. Figure 6(a) shows the equilibrium branch for $\Lambda = 1.5$. The rotund limit D corresponds to a bulged nodiod with $\theta_d = 0$ where constant-volume nonaxisymmetric perturbations are critical. However, at the slender limit, stability is lost to constant-volume axisymmetric perturbations at the volume turning point B where the bridge is a constricted unduloid. The pressure turning points are the constant-pressure stability limits where axisymmetric perturbations are critical. Note that the difference between Q at the maximum and minimum pressure stability limits decreases with increasing Λ. Furthermore, the secondary branch does not exist at this slenderness. At $\Lambda \simeq 1.862$, the two pressure turning points coalesce. The entire branch is unstable to constant-pressure perturbations beyond this slenderness. The secondary branch originates at $\Lambda = \sqrt{3}$ and grows in length with Λ. Equilibrium branches for $\Lambda \simeq 4.4934$ are illustrated in Fig. 6(b). This is the critical slenderness at which cylindrical bridges with a free contact line lose stability to axisymmetric perturbations [38]. The primary branch behaves similarly to the previous case in the rotund and slender limits. Interesting to note is the slender limit where the bridge is a cylinder at the turning point B. Increasing the slenderness beyond $\Lambda \simeq 4.4934$, bulged unduloids become the critical equilibria at the slender limit, while the cylindrical state moves past the turning point to the unstable segment AB. The secondary branch is limited by two pieces-of-sphere states at G and G'. It also crosses the primary branch above the volume turning point. However, this crossing does not correspond to a branch intersection because the equilibrium states corresponding to this (v^*, Q) on the primary and secondary branches are different.

Figure 7 shows typical equilibrium branches for long bridges. When $\Lambda \simeq 4.549$, the primary and secondary branches intersect at a transcritical bifurcation and the $n_w = 1$ and $n_w = 2$ families become connected. The equilibrium state belongs to both $n_w = 1$ and $n_w = 2$ families of equilibria at the intersection. Here the secondary branch intersects the stable

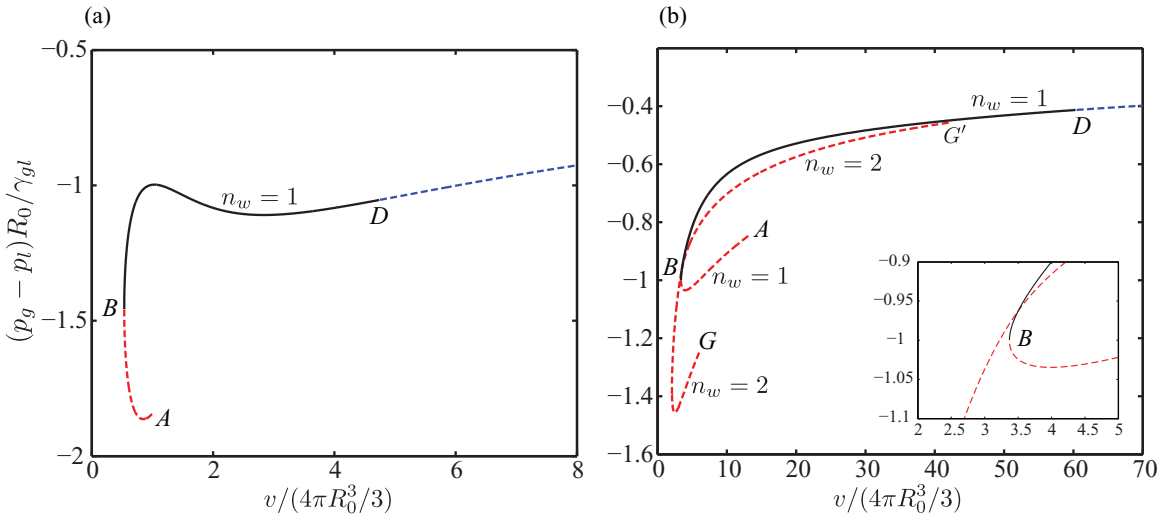

FIG. 6. (Color online) Equilibrium branch for medium-length liquid bridges at fixed slenderness Λ and contact angle θ_c: (a) $\Lambda = 1.5$ and $\theta_c = 90^\circ$ and (b) $\Lambda = 4.4934$ and $\theta_c = 90^\circ$. Stable states (solid) and unstable states (dashed) to axisymmetric (red) and nonaxisymmetric (blue) perturbations are represented for constant-volume perturbations.

part of the primary branch. Increasing Λ by a small value, the $n_w = 1$ and $n_w = 2$ branches split into two half branches, breaking the bifurcation point into two folds (H and H'), as shown in Fig. 7(a). These are turning points in volume. As a result, two disconnected stable branches emerge, which lose stability to constant-volume axisymmetric perturbations at H and H'. These are the points at which $n_w = 1$ and $n_w = 2$ half branches meet. Increasing the slenderness beyond $\Lambda \simeq 4.567$, the stable segment BH disappears, leaving two separate branches with one connected stable segment [see Fig. 7(b)]. Further increase in the slenderness does not affect the behavior of equilibrium branches significantly and constant-volume stability is lost to axisymmetric perturbations at the turning point H' where the bridge is a bulged unduloid. Moreover, the cylindrical state moves from the $n_w = 1$ to the $n_w = 2$ branch at larger slendernesses.

Transcritical bifurcations do not affect the stability region for all contact angles. The secondary branch intersects the stable part of the primary branch when $\theta_c \lesssim 125^\circ$. At larger contact angles, the secondary branch intersects the unstable part below the volume turning point, as illustrated in Fig. 8. When $\theta_c = 120^\circ$, the transcritical bifurcation lies slightly above the turning point on the stable part [Fig. 8(a)]. A small increase in Λ splits the stable part into two disconnected stable segments [Fig. 8(b)]. The smaller stable segment only exists in a narrow range of Λ beyond the transcritical bifurcation and eventually disappears with increasing Λ. Note that the foregoing range becomes larger with decreasing θ_c. However, when $\theta_c = 150^\circ$, the transcritical bifurcation lies below the volume turning point on the unstable part [Fig. 8(c)]. Increasing Λ by a small value splits the unstable part into two disconnected segments, leaving the stable part unaffected [Fig. 8(d)].

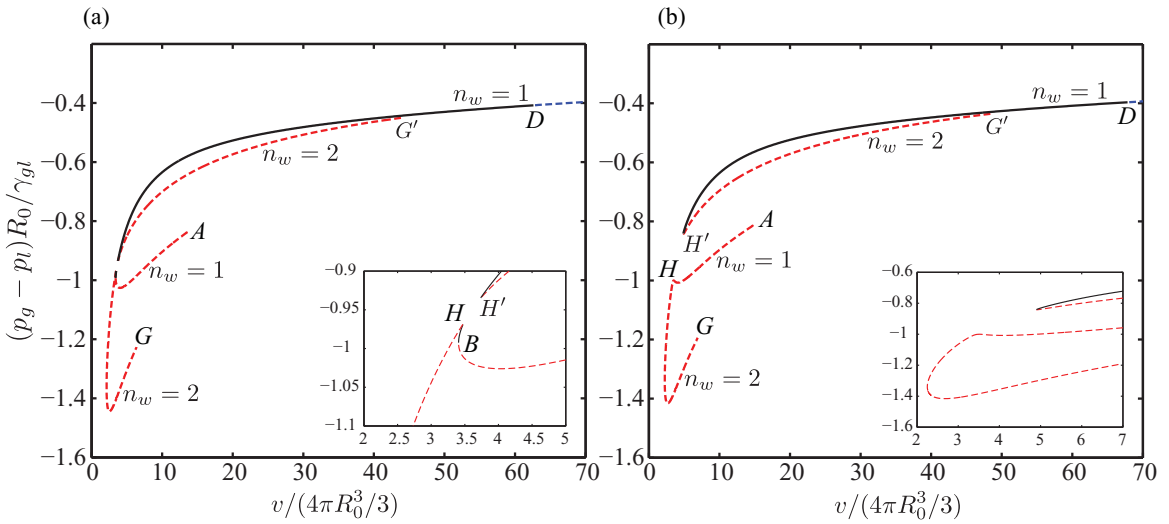

FIG. 7. (Color online) Equilibrium branch for long liquid bridges at fixed slenderness Λ and contact angle θ_c: (a) $\Lambda = 4.555$ and $\theta_c = 90^\circ$ and (b) $\Lambda = 4.57$ and $\theta_c = 90^\circ$. Stable states (solid) and unstable states (dashed) to axisymmetric (red) and nonaxisymmetric (blue) perturbations are represented for constant-volume perturbations.

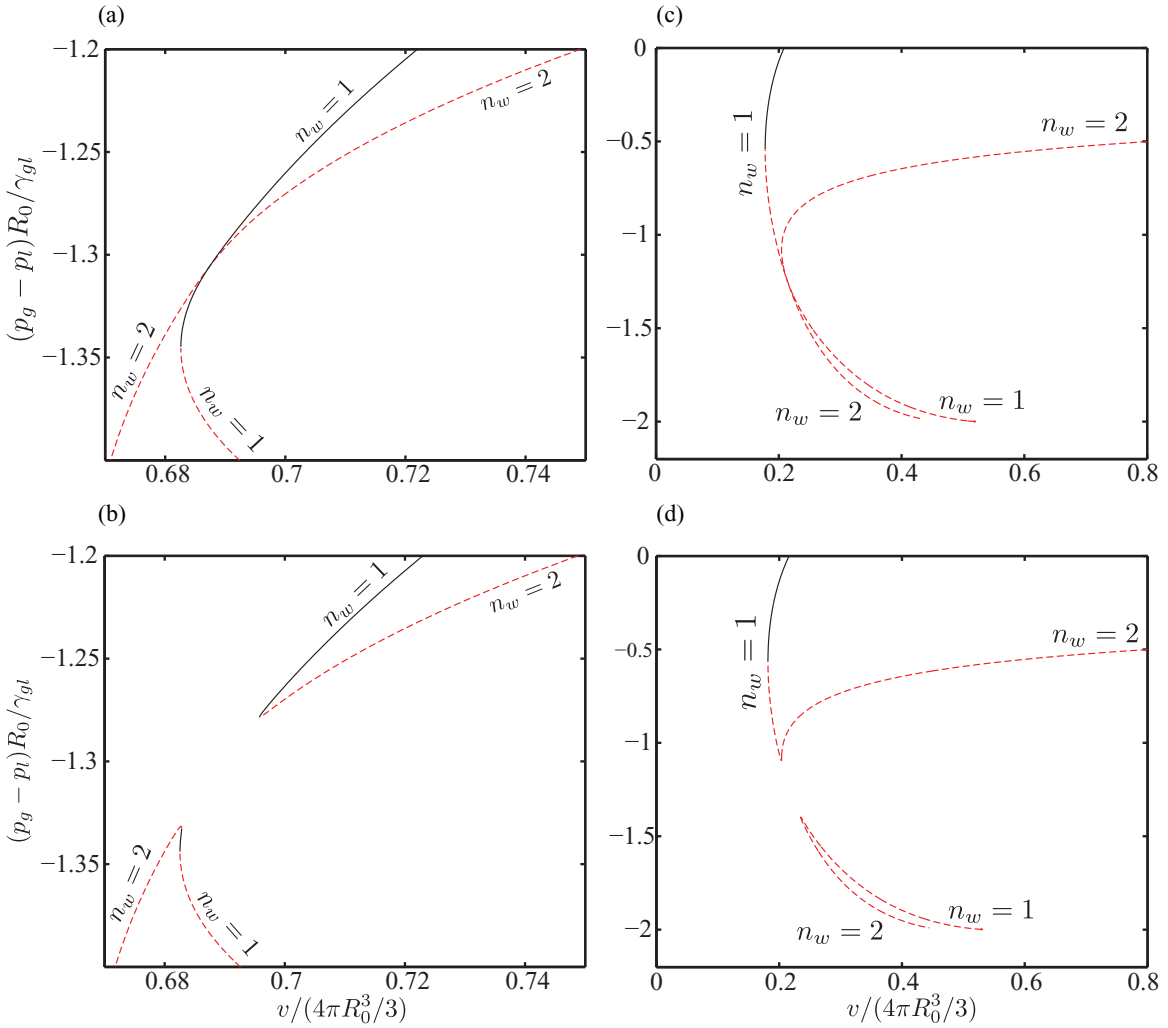

FIG. 8. (Color online) Equilibrium branch in the vicinity of transcritical bifurcations when the slenderness is (a) below ($\Lambda = 2.323$) and (b) above ($\Lambda = 2.325$) the transcritical bifurcation at $\Lambda \simeq 2.3233$ for the contact angle $\theta_c = 120^\circ$, while it is (c) below ($\Lambda = 1.026$) and (d) above ($\Lambda = 1.04$) the transcritical bifurcation at $\Lambda \simeq 1.0285$ for $\theta_c = 150^\circ$. Stable states (solid) and unstable states (dashed) to axisymmetric perturbations are represented for constant-volume perturbations.

D. Stability region

Here we present the stability region in (Λ, V) diagrams for fixed θ_c. Note that equilibrium states are not uniquely specified by the independent parameters $\mathbf{p} = (\Lambda, V, \theta_c)$. Therefore, points inside the stability region in this space may simultaneously correspond to stable and unstable bridges. These parameters nevertheless can be readily measured experimentally, furnishing a convenient representation of the stability limits. We first demonstrate bifurcation characteristics and the critical perturbations along the stability region boundaries for $\theta_c = 90^\circ$ as an example.

Figure 9 illustrates the stability region with respect to constant-volume perturbations for $\theta_c = 90^\circ$. The upper boundary An and the lower boundary for short bridges ABC correspond to nodoids with $\theta_d = 0$ and $\theta_d = \pi$, respectively, where stability is lost at pitchfork bifurcations to nonaxisymmetric perturbations. This behavior is the same as for bridges pinned at two equal disks. However, a detailed bifurcation analysis is required to differentiate between supercritical and subcritical pitchforks along $nABC$ [24,35]. The nodoids belonging to the boundary segment ABC are also the limiting surfaces resulting from the geometric constraint imposed by the disk ($\theta_d \leqslant \pi$). Nodoids are the critical surfaces along the segment CD where stability is lost at turning points to axisymmetric perturbations. The critical surface at D is a catenoid with $\theta_d \simeq 167.8^\circ$. Axisymmetric perturbations are the most dangerous along DE. The critical surface at E is a cylinder with $\Lambda \simeq 4.4934$ corresponding to the stability limit of cylindrical bridges with a free contact line [B in Fig. 6(b)]. This is the point where the line $V = 1$ is tangent to the boundary segment $CDEF$. This line intersects the segment FGm at $\Lambda \simeq 4.5667$. The segment AE of the $V = 1$ line is the locus of stable cylindrical bridges. However, the remaining segment inside the stability region is the locus of stable unduliods with $V = 1$; the cylindrical bridges corresponding to this segment are unstable. This contrasts with the stability region of liquid bridges pinned at two equal disks where the slope of the lower boundary at $(\Lambda, V) = (2\pi, 1)$ is $1/\pi$. Axisymmetric perturbations are critical along $EFGm$. Here, except the point G, which corresponds to a transcritical bifurcation, stability

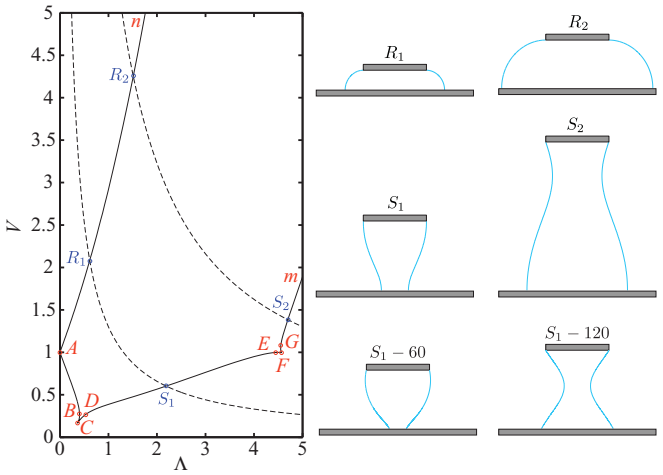

FIG. 9. (Color online) Stability region with respect to constant-volume perturbations with $\theta_c = 90^\circ$. Dashed lines correspond to constant-volume drop dispensing with $v^* = 1$,4.9 (upward). When $v^* = 1$, the bridge profiles at the slender limit for $\theta_c = 60^\circ$ $(S_1 - 60)$ and $\theta_c = 120^\circ$ $(S_1 - 120)$ are shown for comparison.

is lost at turning points. Bifurcation characteristics along the stability-region boundaries are summarized in Table I. As discussed in Sec. III C, the kink EFG is a result of the secondary branch intersecting and splitting the stable part of the primary branch when $4.549 < \Lambda < 4.567$. Note that transcritical bifurcation only occurs at one point along the lower boundary, indicating why transcritical bifurcations are nongeneric and unlikely to be realized in practice.

The upper boundary nA and lower boundary $CDEFGm$ of the stability region (see Fig. 9) are respectively relevant to squeezing and stretching liquid bridges in contact-drop dispensing. For a given bridge volume v and contact angle θ_c, the upper boundary furnishes Λ at the rotund limit where the bridge bugles nonaxisymmetrically upon squeezing; the lower boundary provides Λ at the slender limit where the bridge breaks into two primary drops upon stretching.

Dashed lines in Fig. 9 are the paths corresponding to constant-volume drop dispensing. The bridge interface is deformed into a nonaxisymmetric surface at the rotund limit if the bridge is squeezed, whereas the bridge breaks into two primary drops at the slender limit if it is stretched. The points R_1 (R_2) and S_1 (S_2) correspond to the rotund and slender limits for $v^* = 1$ $(v^* = 4.9)$, respectively. The critical surface is a bulged nodiod with $\theta_d = 0$ at the rotund limit for both paths. However, the slender limit behaves differently for small and large bridge volumes. At small volumes, the drop dispensing path intersects the segment DE where the critical surface is a constricted unduloid, and a neck forms close to the plate, whereas at large volumes the drop dispensing path intersects the segment $EFGm$ where the critical surface is a bulged unduloid, and a neck forms close to the disk. Consequently, the ratio of the dispensed drop volume to the bridge volume in the former case is smaller than in the latter case. A fully dynamic analysis is necessary to precisely quantify this ratio.

When $v^* = 1$, the bridge profiles at the slender limit for $\theta_c = 60^\circ$ $(S_1 - 60)$, $\theta_c = 120^\circ$ $(S_1 - 120)$, and $\theta_c = 90^\circ$ (S_1) are compared in Fig. 9. Here the contact-line radius is smaller and the neck is closer to the plate on more hydrophobic surfaces $(\theta_c < \pi/2)$. This demonstrates how the symmetry-breaking effect of the free contact line can be exploited to dispense smaller drops by adjusting the contact angle. In contrast, liquid bridges between equal disks are inherently reflectively symmetric and uneven breakup is only induced by asymmetric critical perturbations at the slender limit (due to broken equatorial symmetry) at large volumes [35,37]. This result is also helpful for interpreting experimental observations on breakup dynamics in contact-drop dispensing. For example, Qian *et al.* [18] reported very small dispensed drops in a pressure-controlled deposition at fast needle retraction speeds. This can be attributed to an asymmetric breakup of the bridge close to its static slender limit induced by a moving contact line with a small dynamic contact angle. Static stability results in this paper suggest that asymmetric breakups can be induced even in the quasistatic limit by purely geometric means.

The stability region with respect to constant-volume and constant-pressure perturbations is plotted as (Λ, V) diagrams for fixed θ_c in Fig. 10. The constant-volume stability region is an open area, which completely encompasses the constant-pressure stability region at all θ_c. This implies that all the liquid bridges that are stable to constant-pressure perturbations are also stable to constant-volume perturbations, but the converse does not hold. The maximum volume stability limit increases with Λ more rapidly as θ_c increases. The same behavior is observed for the minimum volume stability limit at large slendernesses. Thin solid lines indicate the locus of catenoids $(Q = 0)$ at the respective contact angle. Along these curves, Λ reaches a maximum when intersecting the boundary of the constant-pressure stability region for a fixed θ_c. This point splits the catenoid curve into two segments. The upper

TABLE I. Bifurcation characteristics along the stability-region boundaries in Fig. 9 for the contact angle $\theta_c = 90^\circ$.

Open segment	Critical surface	θ_d	Critical perturbations	Bifurcation type
nA	bulged nodoid	0°	nonaxisymmetric	pitchfork
ABC	constricted nodoid	180°	nonaxisymmetric	pitchfork
CD	constricted nodoid	$(167.8^\circ, 180^\circ)$	axisymmetric	turning point
point D	catenoid	167.8°	axisymmetric	turning point
DE	constricted unduloid	$(81.9^\circ, 167.8^\circ)$	axisymmetric	turning point
point E	cylinder	90°	axisymmetric	turning point
EFG	bulged unduloid	$(90^\circ, 102.3^\circ)$	axisymmetric	turning point
point G	bulged unduloid	102.3°	axisymmetric	transcritical
Gm	bulged unduloid	$(102.3^\circ, 180^\circ)$	axisymmetric	turning point

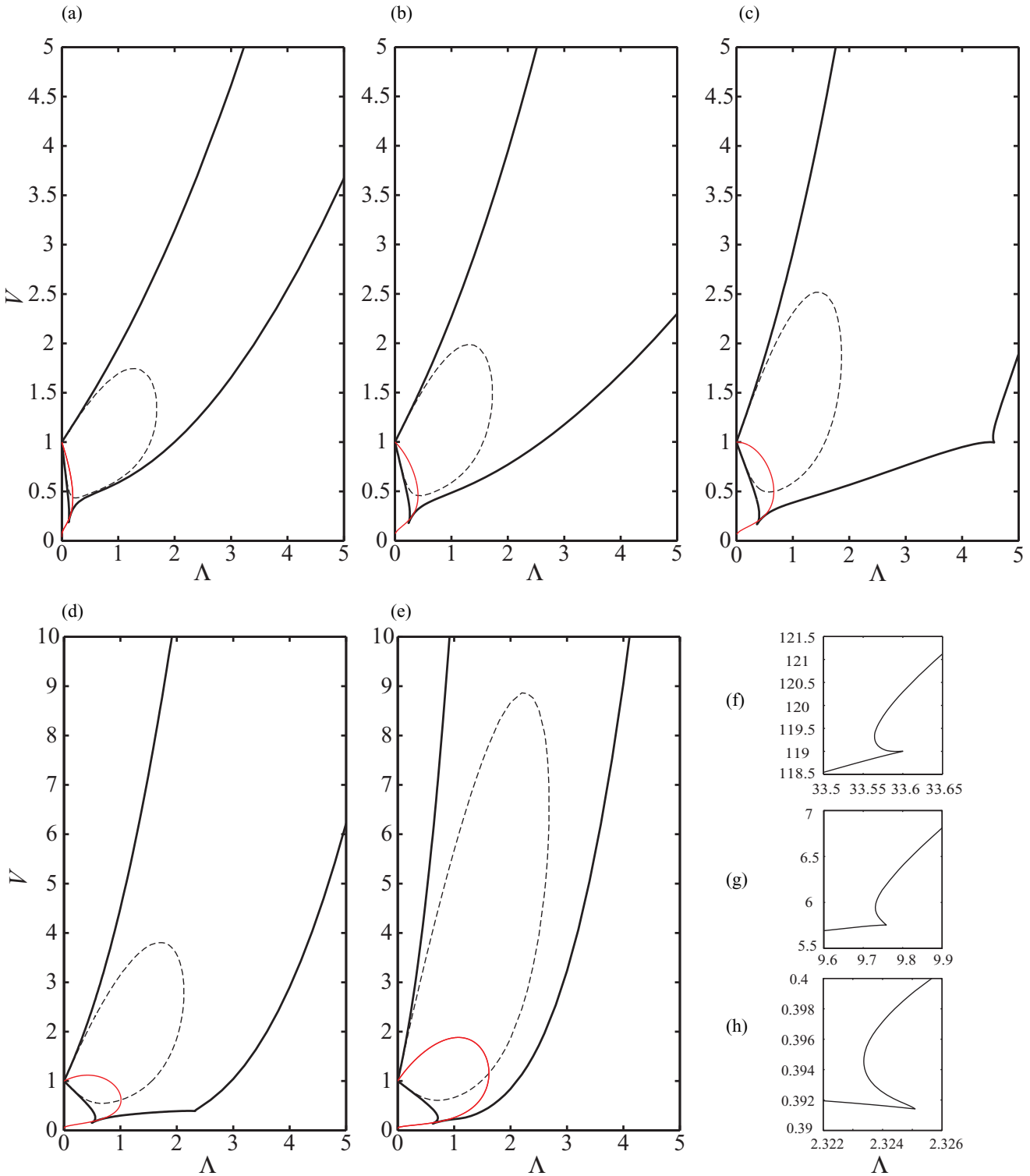

FIG. 10. (Color online) Stability region with respect to constant-volume (thick solid) and constant-pressure (dashed) perturbations with (a) $\theta_c = 30^\circ$, (b) $\theta_c = 60^\circ$, (c) $\theta_c = 90^\circ$, (d) $\theta_c = 120^\circ$, and (e) $\theta_c = 150^\circ$. Thin solid lines indicate the locus of catenoids at the respective contact angle. The lower boundary in the transcritical bifurcation neighbourhood is magnified for (f) $\theta_c = 30^\circ$, (g) $\theta_c = 60^\circ$, and (h) $\theta_c = 120^\circ$.

segment corresponds to stable catenoids, while the lower one corresponds to catenoids that are unstable with respect to constant-pressure axisymmetric perturbations. For a given θ_c, liquid bridges with $Q > 0$ can only correspond to the points inside the region confined between the red curves and the V axis. Furthermore, the kink in the lower boundary that precedes the transcritical bifurcation only exists when $\theta_c \lesssim 125^\circ$ and occurs at larger Λ and V for smaller θ_c.

We conclude this section by comparing the limiting behavior of the maximum and minimum volume stability

limits when $\Lambda \ll 1$ for liquid bridges considered in this study (case I) and those pinned at two equal disks (case II). As previously mentioned, the upper and lower boundaries of the constant-volume stability region, respectively, correspond to bulged nodoids with $\theta_d = 0$ and constricted nodoids with $\theta_d = \pi$ for case I where nonaxisymmetric perturbations are critical. Expanding the cylindrical volume as a power series in slenderness for $\Lambda \ll 1$, we find the approximate expressions

$$\begin{aligned} V = 1 &+ \tfrac{1}{4}\sec^4(\theta_c/2)(\pi - \theta_c + \cos\theta_c \sin\theta_c)\Lambda \\ &- \tfrac{1}{384}\sec^8(\theta_c/2)[-97 + 24(\pi - \theta_c)^2 - 136\cos\theta_c \\ &- 32\cos(2\theta_c) + 8\cos(3\theta_c) + \cos(4\theta_c) \\ &+ 24(\pi - \theta_c)\sin(2\theta_c)]\Lambda^2 + O(\Lambda^3), \end{aligned} \tag{52}$$

$$\begin{aligned} V = 1 &+ \tfrac{1}{4}\csc^4(\theta_c/2)(-\theta_c + \cos\theta_c \sin\theta_c)\Lambda \\ &- \tfrac{1}{384}\csc^8(\theta_c/2)\big[-97 + 24\theta_c^2 + 136\cos\theta_c \\ &- 32\cos(2\theta_c) - 8\cos(3\theta_c) + \cos(4\theta_c) \\ &- 24\theta_c \sin(2\theta_c)\big]\Lambda^2 + O(\Lambda^3) \end{aligned} \tag{53}$$

for the upper and lower boundaries, respectively. These are accurate to second order in Λ and are in good agreement with numerical computations for short bridges (Fig. 11). Letting $\theta_c = \pi/2$, Eqs. (52) and (53), respectively, simplify to

$$V = 1 + \frac{\pi}{2}\Lambda + \left(\frac{8}{3} - \frac{\pi^2}{4}\right)\Lambda^2 + O(\Lambda^3), \tag{54}$$

$$V = 1 - \frac{\pi}{2}\Lambda + \left(\frac{8}{3} - \frac{\pi^2}{4}\right)\Lambda^2 + O(\Lambda^3), \tag{55}$$

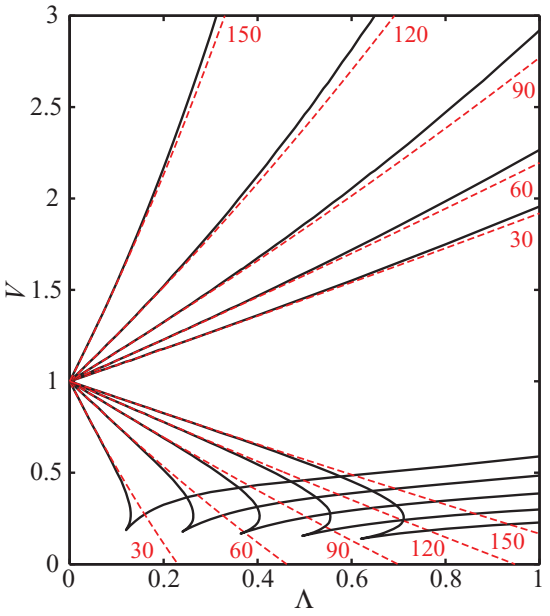

FIG. 11. (Color online) Comparison of approximate formulas (52) and (53) (dashed) and numerical computations (solid) for the upper and lower boundaries of the constant-volume stability region in the small-slenderness limit. Labels denote the contact angle θ_c in degrees.

which are identical to the expressions in the literature for case II [35] with a slenderness twice that of case I. Recall that bulged nodoids with $\theta_d = 0$ and constricted nodoids with $\theta_d = \pi$ are also the critical surfaces along the upper and lower boundaries of the constant-volume stability region for case II. Therefore, when $\theta_c = \pi/2$, a critical surface for case I is half as slender as the corresponding critical surface for case II, while their cylindrical volumes are equal. Consequently, the maximum and minimum volume stability limits of case I for short bridges in a (Λ^I, V) diagram must approach those of case II in a $(\Lambda^{II}/2, V)$ diagram as $\theta_c \to \pi/2$, where Λ^I and Λ^{II} denote the slenderness in cases I and II, respectively.

E. Pinned versus free contact lines

Liquid bridges with two pinned contact lines are exposed to a smaller set of axisymmetric perturbations than those with a free contact line, so the former is more stable with respect to axisymmetric perturbations. Consequently, a fixed-volume liquid bridge with a free contact line can be stretched beyond its slender limit Λ_s if the free contact line is pinned to the plate (see Fig. 1), implying that free contact lines have a destabilizing effect. Figure 12 demonstrates this effect by comparing equilibrium branches at fixed v for a drop bridging a disk and plate (case I), as shown Fig. 1, and two unequal disks (case II), as studied by Slobozhanin *et al.* [26]. The bridge in case I has a pinned and a free contact line, whereas in case II it has two pinned contact lines. Note that cases I and II are, respectively, specified by $\mathbf{p} = (\Lambda, V, \theta_c)$ and (Λ, V, K), where K is the ratio of the lower to upper contact-line diameters. When stretching the bridge, K varies at fixed θ_c in case I and θ_c varies at fixed K in case II. Therefore, comparing the stability of cases I and II is not straightforward.

To explicitly demonstrate the contact-line effect, the same upper disk is used in cases I and II, while the lower disk in case II is chosen to have the same radius as the contact line in case I at its slender limit Λ_s^I (S_1 in Fig. 12). As a result, the bridge profiles for both cases are identical at $\Lambda = \Lambda_s^I$. When $\theta_c = 60^\circ$ and $v^* \simeq 0.3636$, the bridge in case I loses stability to axisymmetric perturbations at S_1 upon stretching, where $\Lambda_s^I = 1$ [Fig. 12(a)]. To accommodate the contact-line radius at S_1 in case I, $K \simeq 0.1870$ in case II. Note that S_1 is not a turning point on the equilibrium branch of case II, so the bridge can be stretched beyond Λ_s^I. The bridge in case II loses stability to axisymmetric perturbations at its slender limit $\Lambda_s^{II} \simeq 1.2281$ (S_2 in Fig. 12), which is well above that of case I. Unlike case I, the rotund limit of case II R_2 is a turning point where axisymmetric perturbations are the most dangerous. This agrees with previous reports in the literature [26] that when $0 < K < 0.306$ the rotund limit is not a pitchfork bifurcation at which nonaxisymmetric perturbations are the most dangerous. Thus, the bridge in case II does not bulge nonaxisymmetrically upon squeezing.

When $\theta_c = 120^\circ$ and $v^* \simeq 2.3455$, the bridge in case I loses stability to axisymmetric perturbations at $\Lambda_s^I = 3$ [Fig. 12(b)] upon stretching. Similarly to Fig. 12(a), the bridge in case II breaks at a higher slenderness ($\Lambda_s^{II} \simeq 3.0697$) than that in case I. However, the rotund limit in both cases is a pitchfork bifurcation where nonaxisymmetric perturbations

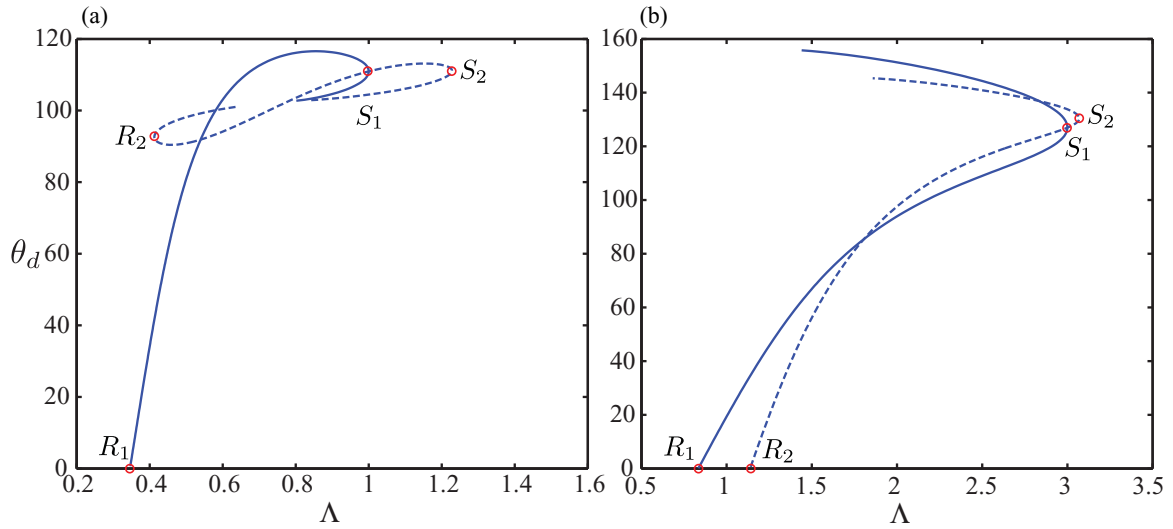

FIG. 12. (Color online) Comparison of equilibrium branches for a liquid bridge, having a free (solid) and pinned (dashed) contact line on the plate with (a) $\theta_c = 60^\circ$, $v^* \simeq 0.3636$, and $K \simeq 0.1870$ and (b) $\theta_c = 120^\circ$, $v^* \simeq 2.3455$, and $K \simeq 1.7461$.

are the most dangerous. Thus, the bridge in cases I and II bulges nonaxisymmetrically upon squeezing.

IV. CONCLUSION

We have examined the equilibrium and stability of weightless liquid bridges that are pinned at one contact line to a disk with the other free to move on a parallel plate. Constant-volume and constant-pressure stability regions were constructed for fixed contact angles. Bifurcations along the stability-region boundaries were determined from the structure of equilibrium branches and families of equilibria. A branch classification was proposed based on the wave number of pieces-of-sphere states at branch terminal points, accounting for the symmetry-breaking role of the free contact line. In comparison with liquid bridges pinned at two equal disks, the free contact line completely breaks the equatorial and reflective symmetries, destroying the pitchfork bifurcations along the lower boundary of the constant-volume stability region where axisymmetric perturbations are critical. This effect, which is of static character, causes liquid bridges to form a neck near the plate before breakup on hydrophobic surfaces ($\theta_c < \pi/2$), leading to small dispensed-drop volumes. Therefore, controlling the drop size by surface hydrophobization can be achieved even in the quasistatic limit, as we have shown via a stability analysis.

Our results can be directly applied to drop deposition on ideal surfaces in the quasistatic limit. However, real surfaces exhibit contact-angle hysteresis. The contact line remains fixed until the advancing (receding) contact angle is reached from above (below) if the bridge is squeezed (stretched). When dispensing drops on real surfaces, perturbations of sufficiently small amplitude do not displace the contact line for contact angles above (below) the advancing (receding) contact angle. When the advancing or receding contact angle is reached, the contact line can freely move on the plate. Therefore, there is a transition in the stability limits between two ideal regimes for contact-drop dispensing on real surfaces: (i) liquid bridges between unequal disks with perfectly pinned contact lines, as studied by Slobozhanin *et al.* [26], and (ii) liquid bridges with a perfectly free contact line, as studied in this paper. For a given advancing contact angle and drop volume, the upper boundary of the stability diagrams in Fig. 10 provides the slenderness at which liquid bridges bulge nonaxisymmetrically. Similarly, for a given receding contact angle and drop volume, the lower boundary of the stability diagrams furnishes the slenderness at breakup. Note that the receding contact angle is constant to a good approximation in the quasistatic phase of drop deposition due to small contact-line speeds. Moreover, the bridge profile and critical perturbations at the slender limit are useful for estimating the dispensed drop size.

Comparing the equilibrium branches of a bridge between a plate and disk and a bridge between two unequal disks revealed the destabilizing effect of a free contact line, which is particularly relevant to breakup at the slender limit. This implies that the breakup height for liquid bridges that are constrained at their contact lines is larger than for those with free contact lines.

ACKNOWLEDGMENTS

This work was supported by the NSERC Innovative Green Wood Fibre Products Network (R.J.H) and the McGill University Faculty of Engineering (McGill Engineering Doctoral Award) (A.A.)

[1] K. Salaita, Y. Wang, and C. A. Mirkin, Applications of dip-pen nanolithography, Nat. Nanotechnol. **2**, 145 (2007).

[2] F. Huo, Z. Zheng, G. Zheng, L. R. Giam, H. Zhang, and C. A. Mirkin, Polymer pen lithography, Science **321**, 1658 (2008).

[3] W. Shim, A. B. Braunschweig, X. Liao, J. Chai, J. K. Lim, G. Zheng, and C. A. Mirkin, Hard-tip, soft-spring lithography, Nature (London) **469**, 516 (2011).

[4] K.-B. Lee, S.-J. Park, C. A. Mirkin, J. C. Smith, and M. Mrksich, Protein nanoarrays generated by dip-pen nanolithography, Science **295**, 1702 (2002).

[5] H.-G. Choi, D.-S. Choi, E.-W. Kim, G.-Y. Jung, J.-W. Choi, and B.-K. Oh, Fabrication of nanopattern by nanoimprint lithography for the application to protein chip, Biochip J. **3**, 76 (2009).

[6] R. Drmanac, A. B. Sparks, M. J. Callow, A. L. Halpern, N. L. Burns, B. G. Kermani, P. Carnevali, I. Nazarenko, G. B. Nilsen, G. Yeung *et al.*, Human genome sequencing using unchained base reads on self-assembling DNA nanoarrays, Science **327**, 78 (2010).

[7] M. García Velarde, *Physicochemical Hydrodynamics: Interfacial Phenomena* (Springer, Berlin, 1988), Vol. 174.

[8] P. G. Smith and T. G. M. van de Ven, The separation of a liquid drop from a stationary solid sphere in a gravitational field, J. Colloid Interface Sci. **105**, 7 (1985).

[9] J. Bico, B. Roman, L. Moulin, and A. Boudaoud, Adhesion: Elastocapillary coalescence in wet hair, Nature (London) **432**, 690 (2004).

[10] H. Kwon, H. Kim, J. Puëll, and L. Mahadevan, Equilibrium of an elastically confined liquid drop, J. Appl. Phys. **103**, 093519 (2008).

[11] L. Giomi and L. Mahadevan, Minimal surfaces bounded by elastic lines, Proc. R. Soc. London Ser. A **468**, 1851 (2012).

[12] A. Akbari, R. J. Hill, and T. G. van de Ven, An elastocapillary model of wood-fibre collapse, Proc. R. Soc. London Ser. A **471**, 20150184 (2015).

[13] J. K. Hwang, S. Cho, J. M. Dang, E. B. Kwak, K. Song, J. Moon, and M. M. Sung, Direct nanoprinting by liquid-bridge-mediated nanotransfer moulding, Nat. Nanotechnol. **5**, 742 (2010).

[14] R. D. Piner, J. Zhu, F. Xu, S. Hong, and C. A. Mirkin, Dip-pen nanolithography, Science **283**, 661 (1999).

[15] J. Eggers and T. F. Dupont, Drop formation in a one-dimensional approximation of the Navier-Stokes equation, J. Fluid Mech. **262**, 205 (1994).

[16] J. Eggers, Nonlinear dynamics and breakup of free-surface flows, Rev. Mod. Phys. **69**, 865 (1997).

[17] S. Dodds, M. da Silveira Carvalho, and S. Kumar, Stretching and slipping of liquid bridges near plates and cavities, Phys. Fluids **21**, 092103 (2009).

[18] B. Qian, M. Loureiro, D. A. Gagnon, A. Tripathi, and K. S. Breuer, Micron-scale droplet deposition on a hydrophobic surface using a retreating syringe, Phys. Rev. Lett. **102**, 164502 (2009).

[19] A. V. Chadov and E. D. Yakhnin, Investigation of the transfer of a liquid from one solid surface to another. I. Slow transfer, Kolloidn. Zh. **41**, 700 (1979).

[20] E. D. Yakhnin and A. V. Chadov, Investigation of the transfer of a liquid from one solid surface to another. II. Dynamic transfer, Kolloidn. Zh. **41**, 1034 (1983).

[21] S. Dodds, M. Carvalho, and S. Kumar, Stretching liquid bridges with moving contact lines: The role of inertia, Phys. Fluids **23**, 092101 (2011).

[22] H. Chen, T. Tang, and A. Amirfazli, Liquid transfer mechanism between two surfaces and the role of contact angles, Soft Matter **10**, 2503 (2014).

[23] R. D. Gillette and D. C. Dyson, Stability of fluid interfaces of revolution between equal solid circular plates, Chem. Eng. J. **2**, 44 (1971).

[24] A. D. Myshkis, V. G. Babskii, N. D. Kopachevskii, L. A. Slobozhanin, A. D. Tyuptsov, and R. S. Wadhwa, *Low-gravity Fluid Mechanics* (Springer, Berlin, 1987).

[25] L. A. Slobozhanin and J. M. Perales, Stability of liquid bridges between equal disks in an axial gravity field, Phys. Fluids A **5**, 1305 (1993).

[26] L. A. Slobozhanin, M. Gomez, and J. M. Perales, Stability of liquid bridges between unequal disks under zero-gravity conditions, Microgravity Sci. Technol. **8**, 23 (1995).

[27] B. J. Lowry and P. H. Steen, Capillary surfaces: stability from families of equilibria with application to the liquid bridge, Proc. R. Soc. London Ser. A **449**, 411 (1995).

[28] L. A. Slobozhanin and J. M. Perales, Stability of an isorotating liquid bridges between equal disks under zero-gravity conditions, Phys. Fluids **8**, 2307 (1996).

[29] L. A. Slobozhanin and J. I. D. Alexander, Combined effect of disk inequality and axial gravity on axisymmetric liquid bridge stability, Phys. Fluids **10**, 2473 (1998).

[30] B. J. Lowry, Fixed boundary dual liquid bridges in zero gravity, Phys. Fluids **12**, 1005 (2000).

[31] J. B. Bostwick and P. H. Steen, Stability of constrained capillary surfaces, Annu. Rev. Fluid Mech. **47**, 539 (2015).

[32] S. Kumar, Liquid transfer in printing processes: Liquid bridges with moving contact lines, Annu. Rev. Fluid Mech. **47**, 67 (2015).

[33] A. Akbari, Wood-fibre collapse upon drying, Ph.D. thesis, McGill University, 2015.

[34] R. U. Seydel, *Practical Bifurcation and Stability Analysis* (Springer, Berlin, 2009).

[35] L. A. Slobozhanin, J. I. D. Alexander, and A. H. Resnick, Bifurcation of the equilibrium states of a weightless liquid bridge, Phys. Fluids **9**, 1893 (1997).

[36] M. J. Russo and P. H. Steen, Instability of rotund capillary bridges to general disturbances: Experiment and theory, J. Colloid Interface Sci. **113**, 154 (1986).

[37] J. Meseguer, L. A. Slobozhanin, and J. M. Perales, A review on the stability of liquid bridges, Adv. Space Res. **16**, 5 (1995).

[38] A. Akbari, R. J. Hill, and T. G. van de Ven, Catenoid stability with a free contact line, arXiv:1505.07159.

[39] D. W. Langbein, *Capillary Surfaces: Shape-Stability-Dynamics, in Particular under Weightlessness* (Springer, Berlin, 2002).

[40] B. Qian and K. S. Breuer, The motion, stability and breakup of a stretching liquid bridge with a receding contact line, J. Fluid Mech. **666**, 554 (2011).

[41] T. I. Vogel, Stability of a liquid drop trapped between two parallel planes, SIAM J. Appl. Math. **47**, 516 (1987).

[42] D. Langbein, Stability of liquid bridges between parallel plates, in *Proceedings of the 8th European Symposium on Materials and Fluid Sciences in Microgravity*, Vol. 1 (European Space Agency, 1992), pp. 85–93.

[43] L. A. Slobozhanin and A. D. Tyuptsov, Characteristic stability parameter of the axisymmetric equilibrium surface of a capillary liquid, Fluid Dyn. **9**, 563 (1974).

[44] J. H. Maddocks, Stability and folds, Arch. Ration. Mech. Anal. **99**, 301 (1987).

[45] I. Martínez and J. M. Perales, Liquid bridge stability data, J. Cryst. Growth **78**, 369 (1986).

[46] L. A. Slobozhanin, J. I. D. Alexander, and V. D. Patel, The stability margin for stable weightless liquid bridges, Phys. Fluids **14**, 209 (2002).

[47] M. J. Marr-Lyon, D. B. Thiessen, F. J. Blonigen, and P. L. Marston, Stabilization of electrically conducting capillary bridges using feedback control of radial electrostatic stresses and the shapes of extended bridges, Phys. Fluids **12**, 986 (2000).

[48] T. I. Vogel, Stability of a liquid drop trapped between two parallel planes II: General contact angles, SIAM J. Appl. Math. **49**, 1009 (1989).